Analysis of the Origin of Atypical Scanning Laser Polarimetry Patterns by Polarization-Sensitive Optical Coherence Tomography

Erich Götzinger,[1] *Michael Pircher,*[1] *Bernhard Baumann,*[1] *Cornelia Hirn,*[2] *Clemens Vass,*[2] *and Christoph K. Hitzenberger*[1]

Purpose. To analyze the physical origin of atypical scanning laser polarimetry (SLP) patterns. To compare polarization-sensitive optical coherence tomography (PS-OCT) scans to SLP images. To present a method to obtain pseudo-SLP images by PS-OCT that are free of atypical artifacts.

Methods. Forty-one eyes of healthy subjects, subjects with suspected glaucoma, and patients with glaucoma were imaged by SLP (GDx VCC) and a prototype spectral domain PS-OCT system. The PS-OCT system acquires three-dimensional (3D) datasets of intensity, retardation, and optic axis orientation simultaneously within 3 seconds. B-scans of intensity and retardation and en face maps of retinal nerve fiber layer (RNFL) retardation were derived from the 3D PS-OCT datasets. Results were compared with those obtained by SLP.

Results. Twenty-two eyes showed atypical retardation patterns, and 19 eyes showed normal patterns. From the 22 atypical eyes, 15 showed atypical patterns in both imaging modalities, five were atypical only in SLP images, and two were atypical only in PS-OCT images. In most (15 of 22) atypical cases, an increased penetration of the probing beam into the birefringent sclera was identified as the source of atypical patterns. In such cases, the artifacts could be eliminated in PS-OCT images by depth segmentation and exclusion of scleral signals.

Conclusions. PS-OCT provides deeper insight into the contribution of different fundus layers to SLP images. Increased light penetration into the sclera can distort SLP retardation patterns of the RNFL. (*Invest Ophthalmol Vis Sci.* 2008;49:5366–5372) DOI:10.1167/iovs.08-2081

Glaucoma is one of the leading causes of blindness in the world.[1,2] The disease causes damage to the retinal nerve fibers. In an early stage of the disease, thinning of the retinal nerve fiber layer (RNFL) can be observed before visual field loss can be detected.[3] Untreated, this thinning leads to irreversible vision loss and finally to blindness. Hence, it is important to detect signs of the disease as early as possible. Scanning laser polarimetry (SLP) is a technique that uses the polarization properties of light to measure the phase retardation induced by the birefringence of the RNFL.[4] This method is essentially based on a confocal scanning laser ophthalmoscope with an integrated ellipsometer. It measures two-dimensional (2D) maps of retardation around the optic nerve head. The latest commercially available SLP system (GDx VCC; Carl Zeiss Meditec, Inc., Dublin, CA) includes a variable corneal compensator to achieve individualized compensation of corneal birefringence. Recent studies have shown that SLP with variable corneal compensation (VCC) improves diagnostic precision compared with SLP with fixed corneal compensation.[5]

However, GDx VCC is known to produce images obscured by artifacts, called atypical scans, in a considerable subset of healthy and glaucomatous eyes.[6–9] Atypical scans show an atypical retardation pattern (ARP) that does not correspond to the RNFL thickness pattern found histologically (in the literature, these patterns have been frequently abbreviated as ABP [atypical birefringence pattern]; however, because SLP measures retardation, not birefringence—which is the quotient of retardation and thickness—we prefer to use the physically correct term, ARP). In addition to high retardation superiorly and inferiorly, scans with ARP display increased retardation in the temporal and nasal quadrants in radial patterns centered on and surrounding the entire optic disc.[7]

The GDx VCC system provides a quantitative scan score, the so-called typical scan score (TSS), which is a quantitative measure for the atypia of the SLP image and is based on a support vector machine analysis.[7] The TSS is derived from the slope, SD, and average magnitude of the RNFL thickness and ranges from 0 to 100, where the lower the score the higher the image atypia. Values of TSS below 80 have been reported to be atypical,[10] and it has been suggested that scans with TSS lower than 60 should be interpreted with care because the diagnostic accuracy might be severely degraded.[11] The reason for ARP is still unknown. It has been hypothesized that such images occur in the presence of low signal-to-noise ratio data resulting from decreased reflectivity of the retinal pigment epithelium.[6] Recent studies showed that ARP can be found in 25% of normal and 50% of glaucomatous eyes and that its presence severely degrades the diagnostic performance of SLP.[6]

Optical coherence tomography (OCT) is a noninvasive imaging technique that generates high-resolution cross-sectional images of transparent and translucent samples.[12–14] OCT provides depth-resolved images of the retina, and, with the use of spectral domain techniques, three-dimensional (3D) volumes of the retina can be imaged within a few seconds.[15,16] However, conventional OCT is limited to measure spatially resolved backscattered intensity. Polarization sensitive (PS)-OCT[17–21] combines the capability of OCT to provide depth information with the polarization sensitivity of SLP. Earlier work demonstrated the value of this technique to provide enhanced image contrast for retinal imaging.[22–25] With PS-OCT, retinal structures could be classified into polarization preserving (e.g., photoreceptor layer), birefringent (e.g., RNFL, Henle fibers),

From the [1]Center for Biomedical Engineering and Physics, and the [2]Department of Ophthalmology, General Hospital and Medical University of Vienna, Vienna, Austria.

Supported by the Austrian Science Fund (FWF Grant P 19624-B02).

Submitted for publication March 27, 2008; revised July 15, 2008; accepted October 8, 2008.

Disclosure: **E. Götzinger**, None; **M. Pircher**, None; **B. Baumann**, None; **C. Hirn**, None; **C. Vass**, None; **C.K. Hitzenberger**, Carl Zeiss Meditec (C)

The publication costs of this article were defrayed in part by page charge payment. This article must therefore be marked "*advertisement*" in accordance with 18 U.S.C. §1734 solely to indicate this fact.

Corresponding author: Christoph K. Hitzenberger, Center for Biomedical Engineering and Physics, Medical University of Vienna, Währinger Strasse 13, A-1090 Vienna, Austria; christoph.hitzenberger@meduniwien.ac.at.

and polarization scrambling or depolarizing (e.g., retinal pigment epithelium [RPE]).[25,26] Moreover, PS-OCT offers quantitative data on the birefringence of the RNFL.[22,27–29]

It is the purpose of this study to analyze the physical origin of atypical SLP patterns. We used PS-OCT to record 3D datasets of backscattered intensity, retardation, and optic axis orientation in eyes with normal retardation patterns (NRPs) and eyes with ARPs. From these datasets, we derived cross-sectional images and en face phase-retardation maps. The results are compared with SLP patterns obtained by GDx VCC in the same eyes. Furthermore, we demonstrate that PS-OCT is capable of obtaining pseudo-SLP images free of atypical retardation artifacts.

Methods

PS-OCT Technology

We used a spectral domain (SD) PS-OCT setup whose technical details are published elsewhere.[24] In brief, light emitted from a superluminescent diode (SLD; center wavelength, 840 nm; bandwidth, 50 nm), after being vertically polarized, illuminates a Michelson interferometer, where it is split by a nonpolarizing beam splitter into a sample and a reference beam. The reference light passes a quarter wave plate (QWP) oriented at 22.5° and is reflected by a mirror. After double passage of the QWP, the orientation of the polarization plane is at 45° to the horizontal, providing equal reference power in both channels of the polarization-sensitive detection unit. The sample beam passes a QWP oriented at 45°, which provides circularly polarized light of 700 μW (well below the safety limits[30,31]) to the eye. The scanning device consists of an *x-y* galvanometer scanner, and through a telescope the pivot point of the scanner is imaged into the pupil plane of the eye. At the interferometer exit, the light is detected with a polarization-sensitive, two-channel detection unit, each channel incorporating a spectrometer. Both spectrometers are identical and consist of a diffraction grating (1200 lines/mm), a lens (f = 200 mm), and a line scan camera (Aviiva M2 CL 2014; Atmel, San Jose, CA).

Our configuration enabled the recording of 20,000 spectra (or A-scans) per second with each camera. Three-dimensional data of the optic nerve head region, covering a scan field of 15° × 15° and consisting of 60 B-scans (1000(x) × 1024(z) pixels), were acquired within 3 seconds. The measured system sensitivity was 98 dB. Theoretic depth resolution within the retina (assuming a refractive index of 1.38) was 4.5 μm. The instrument needs only one measurement per sample location to retrieve information on intensity, retardation, and axis orientation.

Scanning Laser Polarimetry

We used a commercially available SLP instrument with variable corneal compensation (GDx VCC; Carl Zeiss Meditec), details of which have been described in Zhou et al.[32] The instrument essentially consists of a confocal scanning laser ophthalmoscope with an integrated ellipsometer. It measures 2D maps of retardation around the optic nerve head in less than 1 second. The influence of the anterior segment birefringence is compensated individually by measuring the anterior segment birefringence effect in the macula and adjusting a variable retarder to cancel this effect. The measured retardation maps are converted to RNFL thickness maps by use of a constant birefringence value (conversion factor, 0.67 nm/μm) under the assumptions that the RNFL is the only birefringent structure in the area and that the light is backscattered by a polarization-preserving layer.

Patients

All measurements were approved by the ethics committee of the Medical University of Vienna and followed the tenets of the Declaration of Helsinki. Informed consent was obtained from the subjects after explanation of the nature and possible consequences of the study. For this study 11 glaucomatous eyes, 10 healthy eyes, and 20 glaucoma suspect eyes were imaged with PS-OCT and GDx VCC. Patients were selected based on the clinical appearance of the retardation maps on GDx VCC. Healthy eyes had no history of ocular disease apart from refractive error (−2.0 to 0 D). All had intraocular pressure below 21 on Goldmann applanation tonometry, normal appearance of the optic disc on stereoscopic biomicroscopy, and normal visual fields. Glaucoma was defined as glaucomatous optic neuropathy and corresponding (and reproducible) visual field defects. Glaucomatous optic neuropathy was defined as cup-disc asymmetry between the fellow eyes of greater than 0.2, a cup-disc ratio of greater than 0.6, rim thinning, or notching. Visual field abnormality was defined as glaucoma hemifield test results outside normal limits and pattern SD of probability less than 5%. Subjects with suspected glaucoma had the signs of glaucomatous optic neuropathy but visual fields within normal limits.

Based on the pattern of the retardation maps, all subjects were classified twice into either of two groups: normal retardation pattern (NRP) or atypical retardation pattern (ARP). NRP images were defined as retardation maps with low retardation nasally and temporally and the highest retardation superiorly and inferiorly. ARP images were defined as retardation maps with alternating peripapillary circumferential bands of low and high retardation, variable areas of high retardation arranged in a spokelike peripapillary pattern, or splotchy areas of high retardation nasally and temporally.[6] This classification was separately performed for the retardation maps of the GDx by a glaucoma expert and for PS-OCT by a PS-OCT expert. In addition to these subjective classifications, we used the TSS value provided by the GDx VCC as an objective classification means. A TSS value below 80 was considered atypical.

Data Analysis

Three-dimensional PS-OCT datasets of intensity, retardation, and axis orientation were recorded as described.[21,24] From the intensity data, fundus images similar to SLO images were reconstructed by summation of the intensities along each A-scan.[33]

Before the polarization-sensitive data can be further evaluated, they must be corrected for the birefringence of the anterior segment, similar to the case of SLP, to reveal the true birefringent properties of the retina. Given that with PS-OCT we have direct access to the polarization states of the light reflected at arbitrary depths from within the eye, we do not have to rely on retardation values measured in the macular area for that purpose. Instead, we can use directly the retardation and axis orientation measured locally at the retinal surface around the nerve head (which resembles the local anterior segment birefringence) to correct for anterior segment birefringence by a software algorithm. Details of this method have been published elsewhere.[34]

From the corrected 3D retardation dataset, we could derive en face maps of RNFL retardation. Ideally, we would have had to measure the retardation at the posterior RNFL boundary. However, it was difficult to identify the exact location of this boundary, and the signal intensity at this boundary was often weak, which caused noise in polarization-sensitive images. Therefore, we decided to measure the retardation at the posterior boundary of the retina, where the signal was considerably stronger. This choice was based on the assumption that the RNFL is the only birefringent layer in the retina, an assumption that is likely to hold because the Henle fiber layer does not extend to the area around the optic nerve head.

There are three strong reflection sites of approximately equal backscattering strength near the posterior boundary of the retina: the inner/outer photoreceptor junction, the end tips of the photoreceptors, and the RPE.[25,35] These layers are closely spaced and difficult to separate by an automated segmentation algorithm. Given that the last of these layers, the RPE, does not preserve the polarization state of backscattered light but rather depolarizes it (scrambles its polarization state),[25] a simple integration of the retardation values across the three layers would distort the measured retardation, causing it to deviate

Table 1. Classification of Subjects

Subjects	NRP	ARP	Total
Normal	7	3	10
With suspected glaucoma	8	12	20
With glaucoma	6	5	11

Pattern classification based on subjective SLP evaluation.

Table 2. Agreement in and Deviations from Pattern Classification by SLP and PS-OCT

Agreement		Disagreement	
Both NRP	19	ARP in SLP NRP in PS-OCT	5
Both ARP	15	NRP in SLP ARP in PS-OCT	2

from the value induced by the RNFL. To overcome this problem, we used a histogram-based algorithm. First, the complex of the three layers of the posterior retina was segmented in the intensity images (as the first strongly reflecting layer complex below the RNFL). Then we calculated the distribution of retardation values in a window of 50 (depth) × 10 (width) data points that included the three layers. The peak of this distribution was regarded as the corresponding retardation value. This procedure minimizes the influence of the depolarizing RPE because retardation values originating from this layer are randomly distributed. In this manner, we calculated the RNFL retardation for all B-scans of the 3D dataset. As a final processing step, we interpolated values between adjacent B-scans to achieve a grid of 1000 (x) × 650 (y) display points.

To test our hypothesis that increased penetration of the probing light into the birefringent sclera might be the physical reason for the atypical retardation patterns observed in SLP, we used a second evaluation algorithm to calculate birefringence maps from the PS-OCT data. Contrary to OCT, SLP has no depth discrimination and integrates the light backscattered from all depths in the ocular fundus. We simulated this effect in our second algorithm by integrating the data over an extended window depth, again starting at the posterior retinal layer but extending over an entire depth of 450 μm, which now included light backscattered from the sclera. For better comparison with SLP, we did not use the histogram-based algorithm but summed up the signals over the entire window depth along the A-scan (excluding noisy data below a certain intensity threshold). For this method, the retardation at each transverse image point was obtained by the equation

$$\delta = \arctan\left[\frac{\sum A_V(z)}{\sum A_H(z)}\right]$$

where A_V and A_H are the signal amplitudes in the vertical and the horizontal polarization channels and the summation is carried out over the window length of 450 μm (150 data points in depth). Retardation was again calculated, with the same interpolation between B-scans. We use the terms PS-OCT-RL map for the latter method (RL means retardation obtained with the long window) and PS-OCT-RS map for the former method (short window).

Results

The 41 eyes imaged were classified as 10 healthy eyes, 11 glaucomatous eyes, and 20 glaucoma suspect eyes. All eyes were measured with GDx VCC and the PS-OCT system. In all eyes, the two different window-size algorithms were applied on the PS-OCT data, and the results were compared with the SLP measurements. Table 1 shows the distribution of normal and atypical SLP retardation patterns in our study group, as subjectively classified by a glaucoma expert. Agreement with the objective TSS value was excellent. There were only two exceptions, where the subjective classification was ARP although TSS was slightly larger than 80. Agreement between subjective SLP and subjective PS-OCT classification was good, but the judgment deserves some care because PS-OCT is a very new technique and experience in PS-OCT classification is low. In general, PS-OCT images tend to show more atypical areas. In 14 cases, the classification was clearly NRP, in 17 cases clearly ARP, and in 10 cases borderline. Because PS-OCT images tend to be more sensitive to atypia (see the Discussion), we decided to classify the borderline cases that show only weak atypia in PS-OCT as NRP. Based on this classification scheme, Table 2 summarizes agreements and deviations of classifications between SLP and PS-OCT.

Figure 1 shows an NRP compared with an ARP measured with SLP, both obtained from healthy eyes. Black lines indicate the positions of the corresponding B-scans, which are plotted in Figure 2. In Figure 1a, the expected nerve fiber layer retardation pattern, known from histology, can be observed (increased retardation superiorly and inferiorly, indicating thicker RNFL, compared with decreased retardation temporally and nasally, indicating thinner RNFL). In Figure 1b, an atypical SLP retardation pattern can be observed. In addition to high retardation superiorly and inferiorly, also in the nasal and temporal region, areas of increased retardation can be observed that do not match the retardation distribution expected from the anatomic distribution of the retinal nerve fiber layer.

Figure 2 shows intensity and retardation B-scan images measured with PS-OCT in the same eyes at the positions indicated by the black lines in Figure 1. Figures 2a to 2c show intensity images, and Figures 2d to 2f show phase-retardation images of the eye in Figure 1a (NRP). Clearly visible in the intensity images is the first highly backscattering layer that can be associated with the RNFL. The RNFL is thickest superiorly and inferiorly to the nerve head and is thinnest temporally and nasally to the nerve head. In the retardation images 2d to 2f, the increase of retardation with depth caused by the birefringence of the RNFL can be observed. This retardation increase is strongest at the thickest nerve fiber bundles (Figs. 2d, 2f). Figures 2g to 2i show intensity images, and Figures 2j to 2l show phase-retardation images of the eye in Figure 1b (ARP). In addition to retardation induced by the RNFL, a strong increase of retardation can be observed in some areas below the choroid, caused by the birefringent sclera. Comparison with Figure 1b shows that in the corresponding areas atypical retardation is observed.

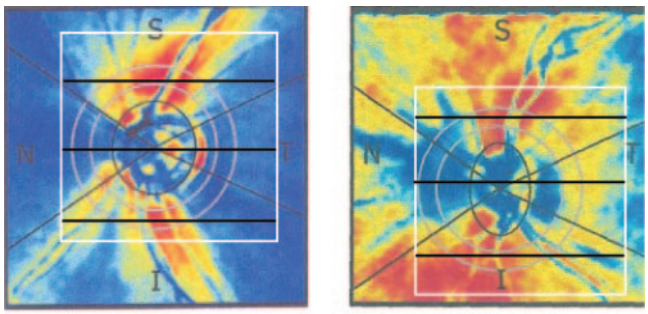

Figure 1. GDx VCC images of healthy eyes. (**a**) Normal retardation pattern (NRP). (**b**) Atypical retardation pattern (ARP). *White rectangles*: areas of PS-OCT en face images (Fig. 3). *Black lines*: traces of PS-OCT B-scans (Fig. 2).

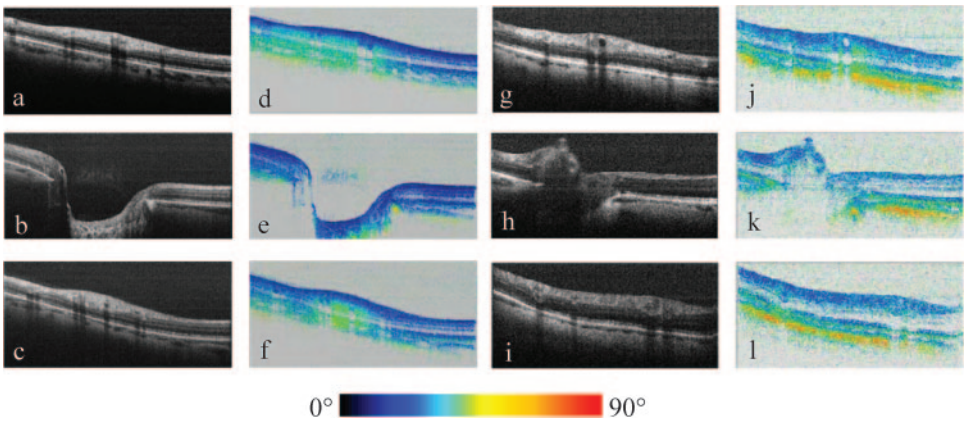

FIGURE 2. PS-OCT B-scan images corresponding to Figure 1. (**a–c**) Intensity images and (**d–f**) retardation images from eye with NRP. (**g–i**) Intensity and (**j–l**) retardation images from eye with ARP.

In Figure 3a, a pseudo-SLO image obtained from the 3D OCT intensity dataset of the normal eye (Fig. 1a) can be seen. The imaged area is indicated by a white rectangle in Figure 1a. Figure 3b shows a retardation map calculated from the 3D PS-OCT dataset in which the large window size (sclera included, PS-OCT-RL) was applied, whereas Figure 3c shows a retardation map calculated with the small window size that excludes the sclera (PS-OCT-RS). Both images show similar retardation patterns and are in good agreement with the SLP image obtained by GDx VCC (Fig. 1a), indicating that scleral influence on the retardation pattern is negligible in this eye. Figure 3d shows a pseudo-SLO image obtained from OCT intensity data of the atypical eye (Fig. 1b). Figures 3e and 3f show PS-OCT-RL and PS-OCT-RS maps, respectively, of the same eye. Whereas Figure 3e shows atypical patches similar to those in the SLP image (Fig. 1b), the atypical areas are essentially removed in Figure 3f, indicating that they were caused by the sclera. The pattern in Figure 3f, therefore, essentially resembles the RNFL distribution.

Figure 4a shows an SLP retardation map obtained in a glaucomatous eye with an atypical birefringence pattern. The black lines indicate the position of the corresponding OCT B-scans (Figs. 4b–4g). Figures 4b to 4d show B-scans of intensity, and Figures 4e to 4g are retardation B-scans. In the intensity images, a pronounced decrease of RNFL thickness and reflectivity can be observed compared with the healthy eye (Fig. 2). In the retardation images, no increase of retardation caused by the RNFL can be observed. Instead, increased penetration into the sclera is observed, together with a retardation increase in these deeper areas. This pronounced scleral influence is observed not only nasally and temporally to the nerve head but also superiorly and inferiorly, mimicking an increased RNFL retardation in the corresponding areas of the SLP map (Fig. 4a).

Figure 5 shows en face images derived from 3D PS-OCT data of the same eye. To cover a larger area of the fundus, four PS-OCT datasets of overlapping areas were recorded in this eye, and the corresponding en face images were mounted to show the wider field of view. The area covered by GDx VCC is indicated by an orange rectangle. Figure 5a is a pseudo-SLO image, and Figures 5b and 5c, respectively, show retardation maps including and excluding the sclera. It can be seen that Figures 4a and 5b exhibit similar retardation patterns. However, Figure 5c reveals that the pattern changes dramatically

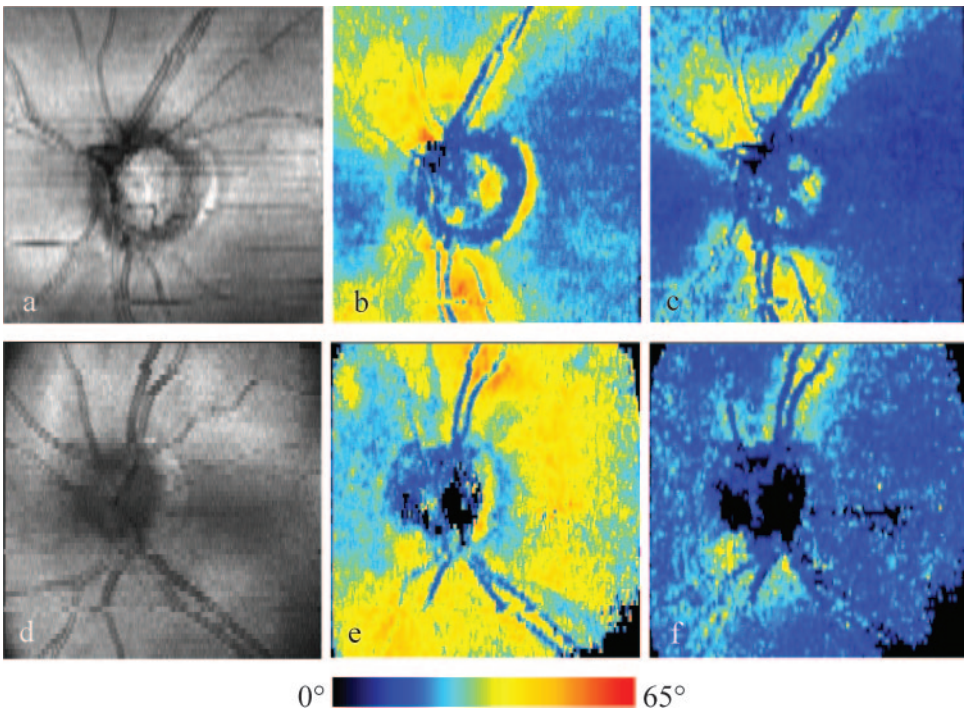

FIGURE 3. PS-OCT en face images corresponding to Figure 1. (**a–c**) NRP. (**d–f**) ARP. (**a**, **d**) Intensity image (pseudo-SLO). (**b**, **e**) Retardation image obtained with large window (PS-OCT-RL). (**c**, **f**) Retardation image obtained with short window (PS-OCT-RS).

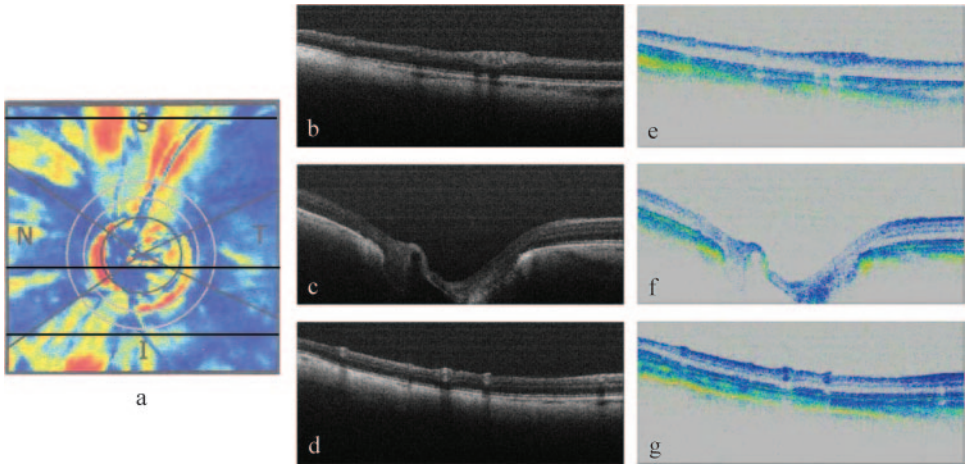

FIGURE 4. Glaucomatous eye with ARP. (**a**) GDx VCC. Traces of B-scans are marked by *black lines*. (**b–d**) Intensity B-scans. (**e–g**) Retardation B-scans. Color bar: see Figure 2.

when the scleral region is excluded. Irregular patches in the nasal and temporal regions are removed. In addition, in the superior and inferior regions, hardly any increase in retardation is visible, indicating that this eye has advanced glaucoma. From the SLP image, this diagnosis was unclear because the strongly birefringent sclera mimicked RNFL retardation.

In most (15 of 22) atypical cases, the increased penetration of probing light into the sclera was identified as the origin of the artifacts. In these cases, it was possible to remove the artifacts with the help of depth segmenting the PS-OCT data (PS-OCT-RS maps). In five cases, atypia was observed in SLP images without scleral influence observed in PS-OCT. In three of these cases, the reason for atypia was probably imperfect corneal compensation. In two cases, atypia was outside the area imaged by PS-OCT, so the origin was unclear. In two other cases, atypia was observed by PS-OCT but not by SLP. The reason seems to be unusually strong depolarization of light at the RPE. Figures 6 and 7 show examples of such cases.

Figure 6 shows a case in which the SLP retardation map (Fig. 6a) and the pseudo-SLP map (PS-OCT-RL, Fig. 6b) are atypical. However, in this case, the atypical patterns in both images have different shapes. Although in the PS-OCT-RL map increased retardation is observed in the inferotemporal and the superonasal regions, the SLP image shows low retardation in these areas. The situation is reversed for the inferonasal and superotemporal regions. We assume that an incorrect corneal compensation was the reason for the distortion of the SLP retardation patterns. The atypia in the PS-OCT-RL map (Fig. 6b) was caused by additional scleral influence, as determined in B-scan images (not shown here).

Figure 7b shows a PS-OCT-RL map with an atypical pattern (increased retardation in several areas), whereas in Figure 7a the SLP map looks normal. No relation to any particular appearance of the fundus on clinical examination was observed. A B-scan (Figs. 7d, 7e) reveals no increased penetration into the sclera. Instead, increased depolarization at the RPE (arrow) added light into the second polarization channel and mimicked birefringence, thereby distorting the birefringence pattern. The depth segmentation (PS-OCT-RS image; Fig. 7c) did not completely remove that artifact.

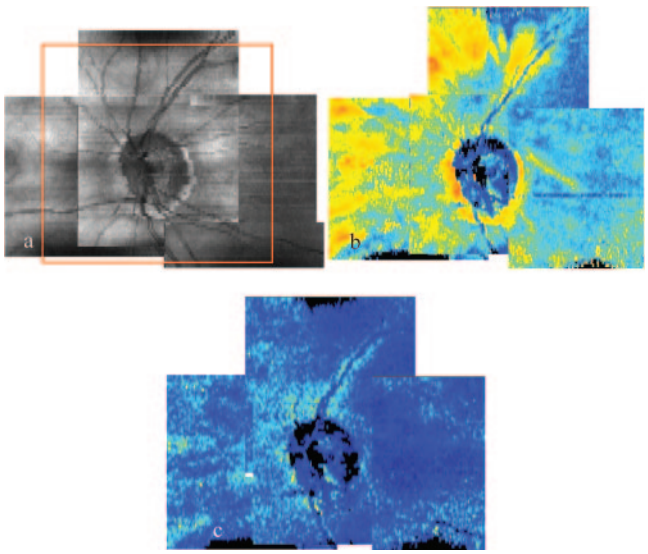

FIGURE 5. PS-OCT en face images corresponding to Figure 4. *Orange rectangle*: area of Figure 4a. (**a**) Intensity (pseudo-SLO). (**b**) Retardation (PS-OCT-RL). (**c**) Retardation (PS-OCT-RS). Color bar: see Figure 3.

DISCUSSION

Atypical RNFL retardation patterns observed in a subset of normal and glaucomatous eyes can confound the RNFL thickness measurement by SLP and reduce the accuracy of glaucoma diagnostics by this technique.[6–8,11] It has, therefore, been suggested that atypical scans should be interpreted with caution in clinical practice. It has been suggested that ARPs are related to age, myopia, and blond fundi and that they may be caused by a low signal-to-noise ratio.[6,8] However, no detailed investigations into the physical origin of ARPs by an independent method have yet been performed. In this study, we used PS-OCT to analyze the physical origin of ARPs. PS-OCT provides 3D datasets of the distribution of phase retardation in the human ocular fundus and of the distribution of the intensity of the backscattered light. PS-OCT can be used to estimate the contribution of light backscattered from various depths to the total retardation map and thereby can provide deeper insight into how the polarizing properties of the different layers in the fundus contribute to the images obtained with SLP.

Our results indicate that in most cases (15 of 22 ARP cases in our study group), atypical retardation patches in SLP images are associated with increased penetration of the probing light beam into the strongly birefringent sclera. Direct comparison between SLP maps by GDx VCC and the corresponding PS-OCT-RL maps that include scleral data show good correlation between atypical patches; however, they are even more pronounced in cases of PS-OCT. The reason is probably a deeper

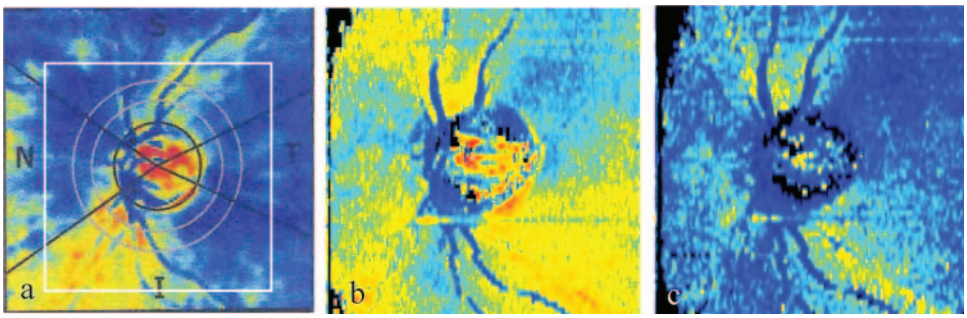

FIGURE 6. Glaucoma suspect eye with ARP, probably caused by imperfect cornea compensation. (**a**) GDx VCC. (**b**) Retardation (PS-OCT-RL). (**c**) Retardation (PS-OCT-RS). Color bar: see Figure 3.

penetration depth for OCT imaging, which we attribute to two factors: the OCT wavelength of 840 nm is less scattered than the somewhat shorter SLP wavelength (785 nm), and the coherent amplification of the OCT detection principle enhances the sensitivity to the weak light intensity backscattered from deeper layers. Taking these considerations into account, we conclude that in most cases, a considerable amount of retardation resulting from the sclera is added to the retardation introduced by the RNFL and thereby generates the atypical patches in the GDx VCC images because this technique has no depth discrimination capability. On the other hand, PS-OCT enables depth segmentation and thereby allows the exclusion of scleral signals in the PS-OCT-RS maps, revealing an undistorted pseudo-SLP map of RNFL birefringence.

In a few cases we observed ARPs without increased penetration into the sclera or where this increased penetration cannot fully explain the observed patterns. In three cases we observed different retardation maps by SLP and PS-OCT-RL. There was a large area of distortion between the retardation patterns that might have been caused by different corneal compensations. If the corneal birefringence is not properly compensated, such large area distortions are expected. GDx VCC measures the corneal birefringence from a retardation pattern in the macular area, whereas PS-OCT uses the retardation pattern measured locally around the nerve head at the retinal surface. If the values in the two areas are different, deviations can occur. Local variation of corneal birefringence has recently been shown to occur in diseases such as keratoconus.[36] Further studies are required to clarify how frequently and by which amount the corneal birefringence influence varies between macula and nerve head locations in a general population.

In two cases, we observed ARPs in PS-OCT images in which SLP maps showed NRPs. In these cases, we observed an abnormally large depolarization at the RPE. This could be caused by a thickened or a more densely pigmented RPE. The abnormally large amount of depolarized light can lead to atypical patterns in the PS-OCT-RL maps because strong polarization scrambling causes more light to be directed toward the vertical polarization channel, increasing the calculated retardation. These atypical patterns might not be fully removed in PS-OCT-RS maps because abnormally broadened histograms of retardation values measured at the posterior retina might shift the histogram peak away from the position corresponding to the true retardation (this effect might also be the cause of the residual retardation occasionally observed temporally and nasally to the optic nerve head in PS-OCT-RS maps; Fig. 5c). More sophisticated segmentation algorithms might be developed that totally exclude the depolarizing RPE from measurement, thus possibly eliminating this error source. On the other hand, the GDx VCC should not be influenced by depolarized light because it uses an algorithm that recognizes depolarization and attempts to exclude it.[32,37]

Apart from analyzing the origin of atypical SLP patterns, PS-OCT might be a useful tool for directly diagnosing glaucoma. Especially in the case of glaucomatous eyes with ARPs, the distorted SLP patterns are difficult to interpret, and the contribution of the birefringent sclera might obscure disturbances of the RNFL. With PS-OCT, it is possible to suppress the influence of the sclera and to reveal the true retardation pattern of the RNFL, which should provide more reliable information on the RNFL state. More work, however, is required to investigate whether PS-OCT can provide improved diagnostic accuracy for glaucomatous eyes with ARP.

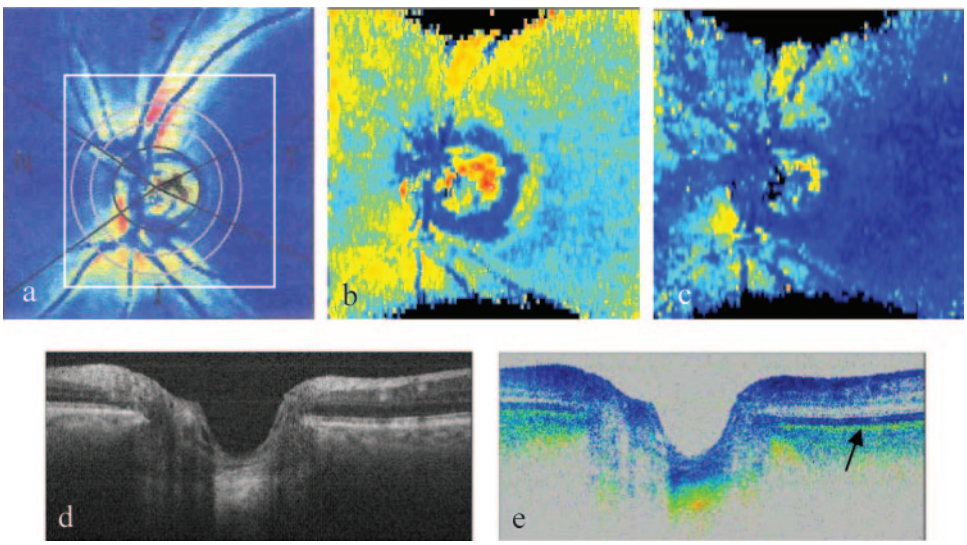

FIGURE 7. Glaucoma suspect eye with NRP in GDx VCC (**a**) and ARP in PS-OCT (**b–e**), probably caused by abnormally strong depolarizing RPE. (**b**) PS-OCT-RL. (**c**) PS-OCT-RS. (**d**) Intensity B-scan. (**e**) Retardation B-scan. *Arrow*: RPE. Color bar for en face PS-OCT: see Figure 3. Color bar for retardation B-scan: see Figure 2.

References

1. Thylefors B, Negrel AD, Pararajasegaram R, Dadzie Y. Global data on blindness. *Bull WHO.* 1995;73:115–121.
2. Quigley HA. Number of people with glaucoma worldwide. *Br J Ophthalmol.* 1996;80:389–393.
3. Quigley HA, Addics EM, Green WR. Optic nerve damage in human glaucoma, III: quantitative correlation of nerve fiber loss and visual field defect in glaucoma, ischemic neuropathy, papilledema, and toxic neuropathy. *Arch Ophthalmol.* 1982;100:135–146.
4. Dreher AW, Reiter K, Weinreb RN. Spatially resolved birefringence of the retinal nerve fiber layer assessed with a retinal laser ellipsometer. *Appl Opt.* 1992;31:3730–3735.
5. Bagga H, Greenfield DS, Feuer W, Knighton RW. Scanning laser polarimetry with variable corneal compensation and optical coherence tomography in normal and glaucomatous eyes. *Am J Ophthalmol.* 2003;135:521–529.
6. Bagga H, Greenfield DS, Feuer WJ. Quantitative assessment of atypical birefringence images using scanning laser polarimetry with variable corneal compensation. *Am J Ophthalmol.* 2005;139:437–446.
7. Bowd C, Medeiros FA, Weinreb RN, Zangwill LM. The effect of atypical birefringence patterns on glaucoma detection using scanning laser polarimetry with variable corneal compensation. *Invest Ophthalmol Vis Sci.* 2007;48:223–227.
8. Mai TA, Reus NJ, Lemij HG. Structure-function relationship is stronger with enhanced corneal compensation than with variable corneal compensation in scanning laser polarimetry. *Invest Ophthalmol Vis Sci.* 2007;48:1651–1658.
9. Sehi M, Ume S, Greenfield DS. Scanning laser polarimetry with enhanced corneal compensation and optical coherence tomography in normal and glaucomatous eyes. *Invest Ophthalmol Vis Sci.* 2007;48:2099–2104.
10. Tóth M, Holló G. Enhanced corneal compensation for scanning laser polarimetry on eyes with atypical polarisation pattern. *Br J Ophthalmol.* 2005;89:1139–1142.
11. Da Pozzo S, Marchesan R, Canziani T, Vattovani O, Ravalico G. Atypical pattern of retardation on GDx-VCC and its effect on retinal nerve fibre layer evaluation in glaucomatous eyes. *Eye.* 2006;20:769–775.
12. Huang D, Swanson EA, Lin CP, et al. Optical coherence tomography. *Science.* 1991;254:1178–1181.
13. Bouma BE, Tearney GJ. *Handbook of Optical Coherence Tomography*. New York: Marcel Dekker; 2002.
14. Fercher AF, Drexler W, Hitzenberger CK, Lasser T. Optical coherence tomography—principles and applications. *Rep Progr Phys.* 2003;66:239–303.
15. Nassif N, Cense B, Park BH, et al. In vivo human retinal imaging by ultrahigh-speed spectral domain optical coherence tomography. *Opt Lett.* 2004;29:480–482.
16. Schmidt-Erfurth U, Leitgeb RA, Michels S, et al. Three-dimensional ultrahigh resolution optical coherence tomography of macular diseases. *Invest Ophthalmol Vis Sci.* 2005;46:3393–3402.
17. Hee MR, Huang D, Swanson EA, Fujimoto JG. Polarization sensitive low coherence reflectometer for birefringence characterization and ranging. *J Opt Soc Am B.* 1992;9:903–908.
18. De Boer JF, Milner TE, Van Gemert MJC, Nelson JS. Two-dimensional birefringence imaging in biological tissue by polarization sensitive optical coherence tomography. *Opt Lett.* 1997;22:934–936.
19. Everett MJ, Schoenenberger K, Colston BW Jr, Da Silva LB. Birefringence characterization of biological tissue by use of optical coherence tomography. *Opt Lett.* 1998;23:228–230.
20. Cense B, Chen TC, Park BH, Pierce MC, de Boer JF. In vivo depth-resolved birefringence measurements of the human retinal nerve fiber layer by polarization-sensitive optical coherence tomography. *Opt Lett.* 2002;27:1610–1612.
21. Hitzenberger CK, Goetzinger E, Sticker M, Pircher M, Fercher AF. Measurement and imaging of birefringence and optic axis orientation by phase resolved polarization sensitive optical coherence tomography. *Opt Express.* 2001;9:780–790.
22. Cense B, Chen TC, Park BH, Pierce MC, de Boer JF. Thickness and birefringence of healthy retinal nerve fiber layer tissue measured with polarization sensitive optical coherence tomography. *Invest Ophthalmol Vis Sci.* 2004;45:2606–2612.
23. Pircher M, Götzinger E, Leitgeb R, Sattmann H, Findl O, Hitzenberger CK. Imaging of polarization properties of human retina in vivo with phase resolved transversal PS-OCT. *Opt Express.* 2004;12:5940–5951.
24. Götzinger E, Pircher M, Hitzenberger CK. High speed spectral domain polarization sensitive optical coherence tomography of the human retina. *Opt Express.* 2005;13:10218–10229.
25. Pircher M, Götzinger E, Findl O, et al. Human macula investigated in vivo with polarization sensitive optical coherence tomography. *Invest Ophthalmol Vis Sci.* 2006;47:5487–5494.
26. Michels S, Pircher M, Geitzenauer W, et al. Value of polarisation-sensitive optical coherence tomography in diseases affecting the retinal pigment epithelium. *Br J Ophthalmol.* 2008;92:204–209.
27. Mujat M, Park BH, Cense B, Chen TC, de Boer JF. Autocalibration of spectral-domain optical coherence tomography spectrometers for in vivo quantitative retinal nerve fiber layer birefringence determination. *J Biomed Opt.* 2007;12:041205.
28. Götzinger E, Pircher M, Baumann B, Hirn C, Vass C, Hitzenberger CK. Retinal nerve fiber layer birefringence measured with polarization sensitive spectral domain OCT and scanning laser polarimetry. *J Biophotonics.* 2008;1:129–139.
29. Yamanari M, Miura M, Makita S, Yatagai T, Yasuno Y. Phase retardation measurement of retinal nerve fiber layer by polarization-sensitive spectral-domain optical coherence tomography and scanning laser polarimetry. *J Biomed Opt.* 2008;13:014013.
30. American National Standards Institute. *American National Standards for Safe Use of Lasers*. Orlando, FL: Laser Institute of America; 2000:ANSI Z 136.1.
31. *Safety of Laser Products*. Geneva, Switzerland: International Electrotechnical Commission; 2006:IEC-60825-1.
32. Zhou Q, Reed J, Betts R, et al. Detection of glaucomatous retinal nerve fiber layer damage by scanning laser polarimetry with variable corneal compensation. *Proc SPIE.* 2003;4951:32–41.
33. Jiao S, Knighton R, Huang X, Gregori G, Puliafito CA. Simultaneous acquisition of sectional and fundus ophthalmic images with spectral-domain optical coherence tomography. *Opt Express.* 2005;13:444–452.
34. Pircher M, Götzinger E, Baumann B, Hitzenberger CK. Corneal birefringence compensation for polarization sensitive optical coherence tomography of the human retina. *J Biomed Opt.* 2007;12:041210.
35. Zawadzki RJ, Jones SM, Zhao M, et al. Adaptive-optics optical coherence tomography for high-resolution and high speed 3D retinal in vivo imaging. *Opt Express.* 2005;13:8532–8546.
36. Götzinger E, Pircher M, Dejaco-Ruhswurm I, Kaminski S, Skorpik C, Hitzenberger CK. Imaging of birefringent properties of keratoconus corneas by polarization-sensitive optical coherence tomography. *Invest Ophthalmol Vis Sci.* 2007;48:3551–3558.
37. Knighton RW, Huang XR. Analytical methods for scanning laser polarimetry. *Opt Express.* 2002;10:1179–1189.